

Bidirectional interconversion of microwave and light with thin-film lithium niobate

Yuntao Xu

Yale University

Ayed Sayem

Yale University

Linran Fan

Yale University <https://orcid.org/0000-0002-5498-7352>

Chang-Ling Zou

Yale university

Sihao Wang

Yale University

Risheng Cheng

Yale University <https://orcid.org/0000-0003-2095-463X>

Wei Fu

Yale University

Likai Yang

Yale University

Mingrui Xu

Yale University

Hong Tang (✉ hong.tang@yale.edu)

Yale University <https://orcid.org/0000-0001-5374-2137>

Article

Keywords: superconducting cavity electro-optics, microwave photons, optical photons

Posted Date: February 25th, 2021

DOI: <https://doi.org/10.21203/rs.3.rs-208781/v1>

License: © ⓘ This work is licensed under a Creative Commons Attribution 4.0 International License.

[Read Full License](#)

Version of Record: A version of this preprint was published at Nature Communications on July 22nd, 2021. See the published version at <https://doi.org/10.1038/s41467-021-24809-y>.

Bidirectional interconversion between microwave and light with thin-film lithium niobate

Yuntao Xu,^{*} Ayed Al Sayem,^{*} Linran Fan,[†] Chang-Ling Zou, Sihao Wang,

Risheng Cheng, Wei Fu, Likai Yang, Mingrui Xu, and Hong X. Tang[‡]

Department of Electrical Engineering, Yale University, New Haven, Connecticut 06520, USA

(Dated: February 4, 2021)

Superconducting cavity electro-optics presents a promising route to coherently convert microwave and optical photons and distribute quantum entanglement between superconducting circuits over long-distance. Strong Pockels nonlinearity and high-performance optical cavity are the prerequisites for high conversion efficiency. Thin-film lithium niobate (TFLN) offers these desired characteristics. Despite significant recent progresses, only unidirectional conversion with efficiencies orders of magnitude lower than expected has been realized. In this article, we demonstrate the first bidirectional electro-optic conversion in TFLN-superconductor hybrid system, with conversion efficiency improved by more than three orders of magnitude. Our new air-clad device architecture boosts the sustainable intracavity pump power at cryogenic temperatures by suppressing the prominent photorefractive effect that limits cryogenic performance of TFLN, and reaches an efficiency of 1.02% (internal efficiency of 15.2%). This work firmly establishes the TFLN-superconductor hybrid EO system as a highly competitive transduction platform for future quantum network applications.

Introduction

With superconducting circuits emerging as a promising platform for quantum computation [1–6] and optical photons being the most suitable long-haul quantum information carrier [7, 8], efficient bidirectional conversion between microwave and optical photons at the quantum level is in critical demand [9–11]. Through high-efficiency electro-optic interface, a hybrid system where quantum information is processed by superconducting circuits and distributed with photonic circuits is one of the most promising schemes to implement large-scale quantum networks [12–16]. Various approaches have realized coherent microwave-to-optical conversion, including spin ensembles [17–20], electro-optomechanics (EOM) [21–30], rare-earth-doped crystal [31, 32], ferromagnetic magnons [33, 34], and etc. The highest conversion efficiency of 47% was demonstrated in EOM systems using bulk optical cavity and free-standing megahertz mechanical membranes [25]. However, it is difficult to operate such transducers at the quantum ground state due to the use of low-frequency mechanical resonators.

The cavity electro-optic (EO) system utilizes the Pockels nonlinearity to realize direct conversion between GHz microwave and optical photons [35–37] without introducing an intermediate excitation. With on-chip frequency tuning, high power handling capability, and robust device design, the highest conversion efficiency for integrated platforms was realized in an Aluminum Nitride cavity EO converter. [38]. Recently, the EO conversion at the microwave ground state has also been demonstrated in a dilution refrigerator at millikelvin temperatures [39, 40].

While promising results have been achieved in AlN EO devices, the relatively weak Pockels effect of AlN makes the further improvement of the conversion efficiency challenging. To tackle this issue, thin-film Lithium Niobate (TFLN) is a promising candidate because of its strong Pockels nonlinearity [41]. This can lead to significantly larger vacuum coupling rate (g_{eo}), which has been demonstrated recently [42, 43]. Nevertheless, the achieved conversion efficiency is limited to $\sim 10^{-5}$, which falls far behind the expectation considering the much larger EO coefficient of LN. It has also been pointed out that the performance of TFLN is largely limited by the prominent photorefractive (PR) effect which is particularly challenging for cryogenic operations. The PR effect constrains the pump power that can be applied to the device. Additionally, the associated charge-screening effect can offset and even cancel the external DC tuning voltage, therefore cause frequency mismatch between microwave resonance and optical mode splitting [44]. As a result, only unidirectional microwave-to-optical conversion has been realized in TFLN EO converters. The bidirectionality of EO conversion process, which is important for two-way quantum networks, remains to be demonstrated.

In this article, we demonstrate a superconducting-photonic hybrid EO converter based on TFLN optical cavities reaching 1.02% on-chip efficiency and 15.2% internal efficiency. The PR effect and its associated charge-screening effects in TFLN are mitigated by a significant margin through utilizing an air-clad device architecture that eliminates the amorphous oxide buffer layer commonly used for as waveguide cladding. This oxide buffer is also employed in previous EO conversion devices to separate superconducting and photonic waveguide structures. The improved efficiency and stability lead to the first demonstration of bidirectional conversion process with TFLN. This buffer-free architecture is also advantageous for future integration with superconducting cir-

^{*} These authors contributed equally to this work.

[†] Current address: College of Optical Sciences, The University of Arizona, Tucson, Arizona 85721, USA

[‡] hong.tang@yale.edu

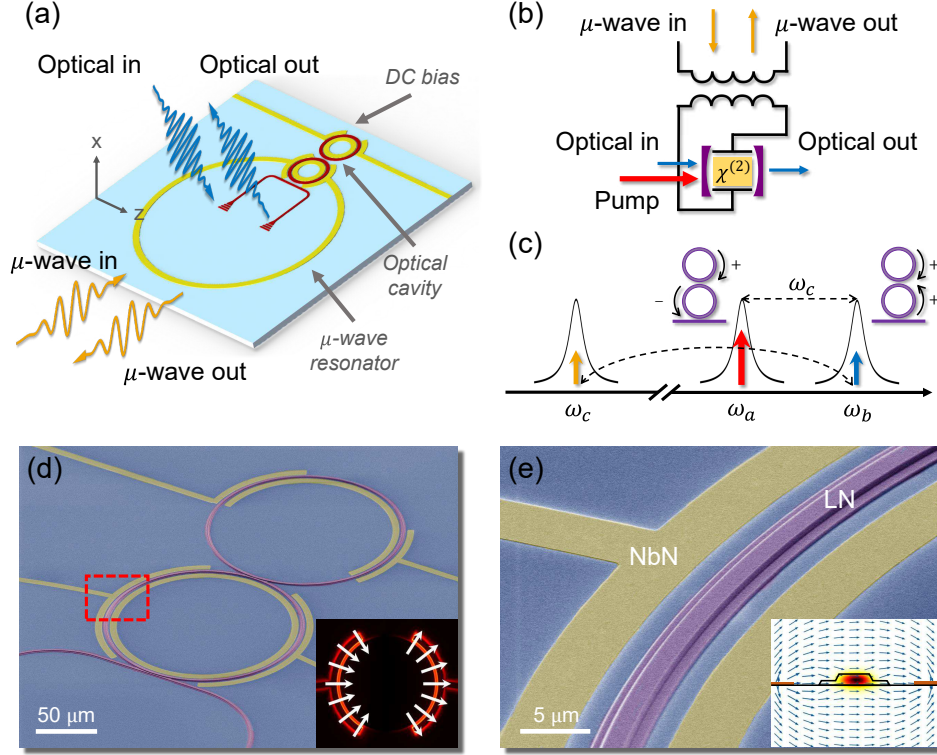


FIG. 1. (a) Schematic layout of the TFLN EO converter, where two strongly coupled microring resonators (red) are co-integrated with an planar superconducting resonator (yellow). DC electrodes are utilized for on-chip tuning of the optical modes. (b) Circuit representation of the cavity EO system. The capacitor plate of the lumped-element microwave resonator is coupled to the $\chi^{(2)}$ optical cavity. (c) Three wave-mixing EO conversion process. The optical doublet corresponds to the symmetric and anti-symmetric supermodes of the coupled microrings. A strong pump (red) at the anti-symmetric mode frequency parametrically stimulates the bidirectional conversion between signal photons in the symmetric mode (blue) and the microwave mode (yellow). (d) and (e) False-color scanning electron microscope images of the EO converter device. Insets show the electric field profiles of interacting optical and microwave modes.

cuits, where amorphous oxides are undesired for their role in hosting two-level systems [45, 46]. The impact of device packaging on the residual RF loss is further examined. We project that with further device improvement in light coupling and cryogenic packaging, the TFLN EO converter could approach unitary internal conversion efficiency, thus enabling a highly competitive transduction platform for future quantum networks.

Result

Figure 1(a) illustrates the schematic layout of our TFLN cavity EO converter, which consists of a pair of strongly coupled ring resonators patterned from x-cut TFLN and a superconducting microwave resonator of Niobium Nitride (NbN). The microwave resonator capacitively couples to one of the double rings for EO conversion, while a pair of DC electrodes is coupled to the other microring for electrical tuning of the optical resonance modes. The circuit representation of the cavity EO system is illustrated in Fig. 1(b), where the electric field of a lumped-circuit LC resonator overlaps with the optical cavity field within the LN EO media through Pockels ef-

fect. As a result of the cavity-enhanced EO interaction at the triply-resonant condition, the input microwave field modulates the optical pump and produces an optical sideband at the signal mode frequency. Reversely, a microwave field output can be generated by the optical frequency mixing in the LN cavity.

This triply-resonant enhanced EO conversion scheme, as illustrated in Fig. 1(c) in frequency domain, is described by an interaction Hamiltonian $H_I = \hbar g_{eo}(ab^\dagger c + a^\dagger bc^\dagger)$. Here, a , b and c denote annihilation operators for the optical pump, signal and microwave modes, respectively. g_{eo} denotes the vacuum EO interaction strength, which in turn is determined by the mode volume, triple-mode overlap and the Pockels coefficient. The optical frequency doublet (Fig. 1(c)) corresponds to the symmetric and anti-symmetric supermodes of the photonic molecule [47] induced by the strong mutual coupling between the fundamental transverse electric (TE) modes of the double-microring resonators [48]. To leverage the highest EO coefficient $r_{33} \sim 30$ pm/V in x-cut TFLN [41], microwave mode with in-plane electrical field is utilized. The corresponding microwave and optical mode profiles

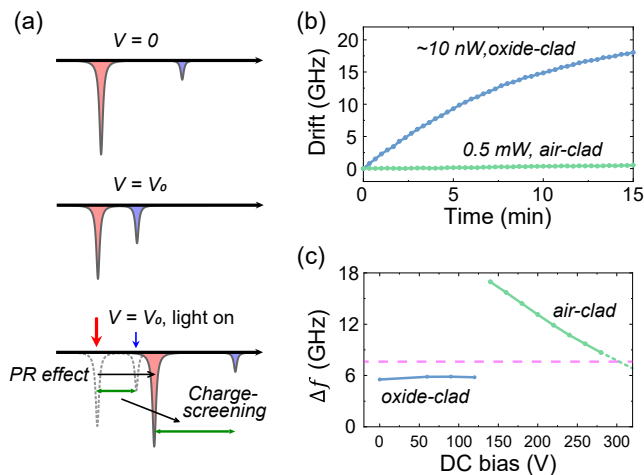


FIG. 2. (a) Illustration of the PR-induced resonance instability resulting from a combination of absolute frequency shift and cancellation of voltage tunability after illumination. (b) The measured resonance frequency shift at zero-bias voltage after light illumination of oxide-clad (blue) and air-clad (green) architecture. (c) The optical supermode splitting Δf as a function of DC bias for oxide-clad (blue) and air-clad (green) devices. The target microwave frequency is marked as a dashed line.

are shown in the insets of Figs. 1(d) and (e).

To initiate quantum frequency conversion, the lower-frequency supermode in the photonic molecule, i.e. the anti-symmetric optical mode a , is loaded with a strong pump to produce a photon-number enhanced electro-optical linear conversion. The advantage of the cavity enhanced coherent conversion is quantified by the cooperativity $C = 4n_p g_{eo}^2 / \kappa_b \kappa_c$, where n_p is the intracavity pump photon number and κ_b , κ_c are the total energy loss rates for modes b and c , respectively. By applying a DC bias through the electrode, the frequency splitting of the optical doublet can be tuned to match the microwave resonance frequency, and fulfill the triply-resonant condition ($\omega_a + \omega_c = \omega_b$). Under this ideal condition, the on-chip peak conversion efficiency is given by,

$$\eta = \frac{\kappa_{b,ex} \kappa_{c,ex}}{\kappa_b \kappa_c} \frac{4C}{(1+C)^2}. \quad (1)$$

Here, $\kappa_{b,ex}$ ($\kappa_{c,ex}$) is the external loss rates for mode b (c), and $\eta_{\text{int}} = 4C/(1+C)^2$ is the internal conversion efficiency. Optimal conversion is achieved when $C = 1$, and the corresponding on-chip efficiency is eventually limited by the extraction ratio $\kappa_{b,ex} \kappa_{c,ex} / \kappa_b \kappa_c$.

As indicated by Eq. 1, the EO conversion efficiency η increases with the pump photon number. On the TFLN platform, the strong PR effect places a limit on achievable intracavity pump power [42, 43]. The PR effect not only destabilizes cavity resonances but also leads to a charge-screening effect which neutralizes the dc-bias field used for tuning the resonances [44]. The PR effect in LN results from a combination of cascaded processes that first

builds up a space-charge field in presence of light illumination and subsequently modulates the refractive index of the material [41]. An illustration of the resonance instability is shown in Fig. 2(a). Unique to the cryogenic temperatures, the relaxation time of the PR effect is found to be extremely long [49], leading to an accumulated space-charge field that semi-permanently shift the resonance frequency. Because of the charge accumulation and the strong photovoltaic dynamics, this screening effect could not be compensated through the regular feedback technique, as the tuning voltage required for phase matching will continuously increase and finally lead to an electrical breakdown of the material.

We found that the PR effect and the charge-screening effect are highly related to the converter design as well as the treatment of LN material. The LN-oxide top-cladding interface is identified to be the major source that aggravates the PR effect [50]. With an air-clad architecture (false color scanning electron microscope images shown in Figures 1(d) and (e)), the detrimental PR effect and charge-screening effect at cryogenic temperature can be effectively mitigated. In our final converter device, the absolute resonance shift induced by the PR effect is reduced by a significant margin (Fig. 2(b)), thus fully compensated for by a slow feedback to allow the drive laser to follow the resonance frequency. A large intracavity photon number can be maintained with stable alignment achieved between the optical supermode splitting Δf and the microwave resonance frequency (Fig. 2(c)). This new air-clad architecture not only enables long-time stable operation of TFLN transduction devices at cryogenic temperatures; it will also benefit future integration of superconducting qubits because the amorphous oxide buffer is known to host the two-level-systems that impact the qubit coherence [45, 46].

The optical components of the converter are patterned from 600 nm-thick x-cut TFLN on sapphire substrate, where 350 nm of TFLN being etched to define the resonators and waveguides. The majority of remaining 250 nm TFLN slab is removed in a second etching step in order to minimize the total coverage of TFLN, leaving only a narrow pedestal to support the microring resonators. This is a crucial step to suppress the microwave loss induced by the strong piezo-electricity of LN. After patterning the optical structures, superconducting NbN is directly deposited on the sapphire substrate using atomic layer deposition (ALD), and then etched to form the microwave resonator and tuning electrodes. With our air-clad architecture, the superconductor traces are also designed to capacitively couple across the waveguides without climbing over the photonic waveguides, thus significantly reducing the fabrication complexity.

The schematic measurement setup for EO conversion is presented in Fig. 3(a). The device is loaded in a closed-cycle refrigerator (Cryomech) cooled down to 1.9 K base temperature. A tunable telecom laser (Santec 710) amplified by erbium-doped fiber amplifier (EDFA) is tuned to the anti-symmetric mode (lower frequency supermode)

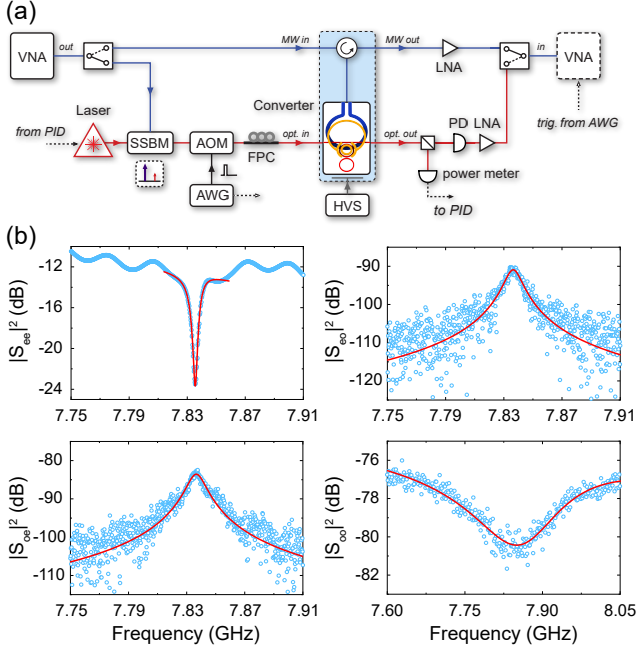


FIG. 3. (a) Measurement setup. The output of a vector network analyzer (VNA) is sent to the device either as the microwave input or as the optical input through a single-sideband modulator (SSBM). For quasi-CW measurements, the pump is gated by an acoustic-optic modulator (AOM) driven by an arbitrary wave generator (AWG), which also triggers VNA. The pump is locked to the optical cavity with a PID controller. FPC: fiber polarization controller. PD: photodetector. LNA: low-noise amplifier. HVS: high voltage source. (b) Measured microwave reflection S_{ee} , optical-to-microwave conversion S_{eo} , microwave-to-optical conversion S_{oe} and optical reflection S_{oo} . The peak pump power is -12.0 dBm in the waveguide and all matrix coefficients are normalized to the VNA output.

as a parametric pump. A pair of grating couplers designed for TE polarized light is used to couple light in and out the device. 1% of the transmitted light from the device is sampled to provide feedback to the laser wavelength through its build-in piezo. RF signal from a vector network analyzer (VNA) is either directly sent to the device as the microwave signal input or used to generate the optical signal input through optical single-sideband modulation [38]. The microwave signal is read-out wirelessly by terminating a coaxial cable with a hoop antenna [19, 40] which inductively couples to the superconducting resonator. The microwave output from the converter is analyzed after a low-noise amplifier at the room temperature. The optical output is collected and down-converted through heterodyne with the pump laser by a high-speed photodetector and then sent to the VNA. For measurement in the high power regime (> -2 dBm), the thermal load to the device is reduced by gating the pump light using a high extinction acoustic-optic modulator (AOM) driven by an arbitrary waveform generator

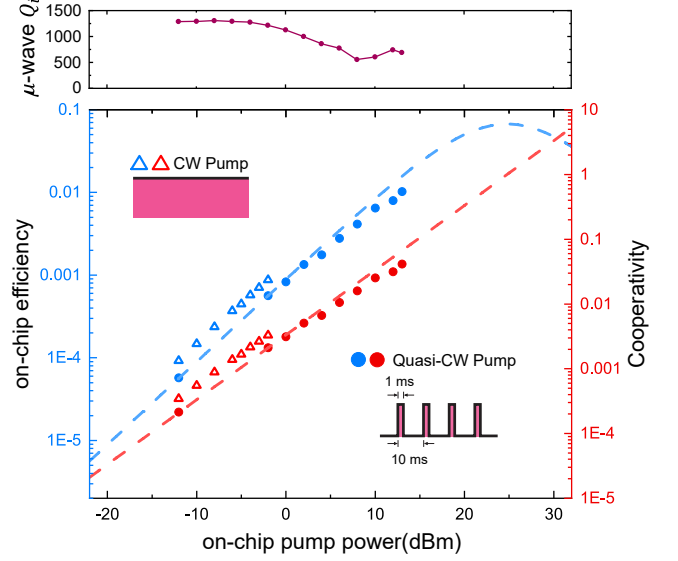


FIG. 4. On-chip conversion efficiency (blue) and cooperativity (red) as a function of the peak pump power in the input waveguide. The discontinuity in the CW and pulsed pump data is due to switching to different pairs of optical modes during the measurements. The maximum conversion efficiency is recorded with a peak pump power of 13.0 dBm. The dashed lines are the theoretical predictions obtained from the data measured with a pulsed pump. The measured intrinsic microwave Q under different optical pump powers are presented in the upper panel.

(AWG).

With a DC bias of 220 V, the optical mode splitting is tuned (at a rate of ~ 0.6 pm/V) to match the microwave resonance frequency. Figure 3 shows the full spectra of scattering matrix elements employed for calibrating the conversion efficiency: optical reflection S_{oo} , microwave reflection S_{ee} , microwave-to-optical conversion S_{oe} and optical-to-microwave conversion S_{eo} . The bidirectional nature of the EO conversion is thus fully established. The Lorentzian fit of the S_{oe} and S_{eo} spectral yield a 3 dB bandwidth matching the microwave linewidth. The peak conversion efficiency is obtained by calibrating out the off-chip gain and loss factor of each input and output signal path [23]:

$$\eta = \frac{S_{eo,p} S_{oe,p}}{S_{oo,bg} S_{ee,bg}}, \quad (2)$$

where $S_{oe,p}$ and $S_{eo,p}$ are the peaks of conversion spectra, $S_{oo,bg}$ and $S_{ee,bg}$ are the backgrounds of reflection spectra, respectively.

The on-chip pump power is gradually increased from -12.0 dBm with the conversion efficiency measured at each step using above-mentioned calibration procedure. Considering the loss and coupling characteristics of microwave and optical cavities, the internal conversion efficiency η_{int} and thus cooperativity C from Eq. 1 under different pump power is extracted, as shown in Fig. 4. At

TABLE I. Device parameters

	frequency $\omega/2\pi$	total loss rate $\kappa/2\pi$	external loss rate $\kappa_{ex}/2\pi$
Pump mode <i>a</i> (CW)	193.34 THz	301 MHz	109 MHz
Signal mode <i>b</i> (CW)	193.35 THz	173 MHz	33 MHz
Pump mode <i>a</i> (quasi-CW)	192.83 THz	380 MHz	124 MHz
Signal mode <i>b</i> (quasi-CW)	192.84 THz	280 MHz	52 MHz
MW mode <i>c</i>	7.836 GHz	9.06 MHz	3.22 MHz

higher pump power levels (> -2.0 dBm), in order to reduce the thermal load to the fridge, We switch to 10% duty cycle quasi-CW pump. After extended exposure during CW measurement, the pair of optical modes we used are no longer accessible due to the accumulated charges. Therefore, we select another pair of optical modes (within the same device) in the quasi-CW measurement, leading to a discontinuity in the data trace. The detailed device characteristic is presented in Table I.

A maximum on-chip conversion efficiency of 1.02% (internal efficiency of 15.2%) is recorded with a peak pump power adjusted to 13.0 dBm in the waveguide. The corresponding cooperativity reach a value of 0.041, which is significant improved over previously obtained values [42, 43]. We note that the cooperativity no longer increases linearly with peak pump power in high power regime. This is attributed to the quality factor degradation of the superconducting resonator, as shown in the upper panel of Fig. 4. From a linear fitting (dashed lines) in Fig. 4(a) of the conversion efficiency in the low power regime, the vacuum coupling rate is estimated to be $g_{eo} = 2\pi \times 750$ Hz, which is within the same order of magnitude compared to simulated value ($2\pi \times 1.5$ kHz) [38].

Discussion. The conversion performance of our current device is mostly limited by the relatively low microwave microwave quality factor. The source of the residual microwave loss could be a combination of light absorption of the superconductor, thermo-optic heating, and undesired coupling from cryogenic measurement. In particular, we found that the microwave Q is significantly affected by how the device is assembled for cryogenic operation. When the device is characterized in a RF tight, compact cooper box package which suppresses the undesired microwave modes from coupling to the on-chip resonator, the device exhibits an intrinsic Q of 9.7×10^3 at 2.6 K, with the microwave reflection spectrum shown in Fig. 5 (trace A). The microwave Q measured here, which shows significantly higher value compared to prior works, is most likely already limited by the dielectric and piezoelectric coupling loss induced by the residual TFLN traces supporting optical waveguides. The wire bonds used for dc-tuning further contribute to microwave loss. As indicated by trace B shown in Fig. 5, when measured with wire bonds in the same closed box at 2.6 K, the intrinsic Q is reduced by almost a half to 5.4×10^3 .

With the final EO conversion package, additional mi-

crowave loss arises from the cryogenic optical interfaces required to accommodate the fiber array. The fiber array is manipulated by a set of attocubes for precision alignment, preventing the use of a fully closed copper box. A copper box with open lid is utilized instead, similar to the configuration previously used in AlN microwave-to-optics experiment [38] where we did not observe significant Q change before and after packaging. However, this is not the case for the TFLN converter studied here. As shown in Fig. 5 (trace C), the device exhibits a further degradation of microwave quality factor, and the extracted intrinsic Q drops to 1.3×10^3 . We conjecture that the excess microwave loss is mainly induced by the stronger piezoelectric coupling of LN (than AlN) to spurious modes supported by the RF packaging. To mitigate this loss, it is critical to further reduce the TFLN trace volume that does not participate in the EO conversion, and utilize a RF packaging that can effectively suppress spurious modes.

It is anticipated that unitary internal conversion efficiency ($C = 1$) can be obtained at the current pump power level, if the intrinsic Q of $\sim 10^4$ can be recovered. With improved cryogenic packaging to suppress parasitic losses. Also, the on-chip efficiency could be further improved by engineering the external loss rate of optical and microwave modes. Our current devices use grating couplers which introduce an insertion loss as high as 12.0 dB per facet due to weak index contrast between LN and sapphire substrate. By utilizing side-coupled inverted

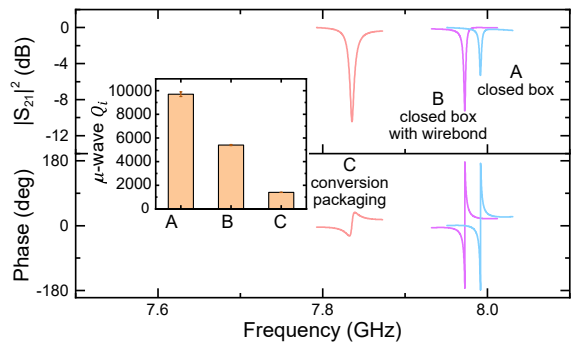


FIG. 5. Microwave reflection spectrum of the device (A) in a closed copper box (B) in a closed copper box with wire bonds (C) packaged with fiber-array for conversion measurement. The inset shows the fitted intrinsic microwave quality factors.

tapers, the insertion loss could be reduced to 3.4 dB per facet [40, 51], which will also dramatically reduce the thermal-optic heating and light absorption induced by scattered light.

We note that the microwave resonator is not at its ground state (thermal photon occupancy $\bar{n}_{\text{th}} \sim 5$) in this work. Characterization of ground state conversion will be done either in a dilution refrigerator at millikelvin temperature [40] or through a radiative cooling technique with improved microwave Q [52]. By then, it is feasible to utilize TFLN-based devices for entanglement distribution via the heralded entanglement generation between microwave and optical photons with blue-detuned pump pulses and photon-counting setup [53, 54].

In conclusion, we demonstrate cavity EO converter based on TFLN with conversion efficiency up to 1.02%, which represents a significant improvement over previous works. Utilizing a air-clad architecture to mitigate the PR effect, the device maintain stable device operation while supporting high pump photons numbers at cryogenic temperatures. This not only allows us to demonstrate bidirectional conversion with high efficiency, but also points to the possible use of cryogenic TFLN de-

vices for quantum applications such as verification of non-classical correlation, generation of entangled photon pairs and etc., which all require extensive stable operation. The system efficiency of the converter can be further improved by proper cryogenic packaging and light coupling. With these improvements, we anticipate to achieve high conversion efficiency with sufficiently low pump power for ground state operation at millikelvin temperature for critical quantum network demonstrations.

Funding. This work is funded by ARO under grant number W911NF-18-1-0020. HXT acknowledges partial supports from NSF (EFMA-1640959), ARO (W911NF-19-2-0115) and the Packard Foundation. Funding for substrate materials used in this research was provided by DOE/BES grant under award number DE-SC0019406.

Acknowledgements. The authors thanks Michael Rooks, Yong Sun, Sean Rinehart and Kelly Woods for support in the cleanroom and assistance in device fabrication.

Disclosures. The authors declare no conflicts of interest.

-
- [1] J. Clarke and F. K. Wilhelm, *Nature* **453**, 1031 (2008).
- [2] M. H. Devoret and R. J. Schoelkopf, *Science* **339**, 1169 (2013).
- [3] P. Kurpiers, P. Magnard, T. Walter, B. Royer, M. Pechal, J. Heinsoo, Y. Salathé, A. Akin, S. Storz, J.-C. Besse, *et al.*, *Nature* **558**, 264 (2018).
- [4] K. S. Chou, J. Z. Blumoff, C. S. Wang, P. C. Reinhold, C. J. Axline, Y. Y. Gao, L. Frunzio, M. Devoret, L. Jiang, and R. Schoelkopf, *Nature* **561**, 368 (2018).
- [5] Y. Zhong, H.-S. Chang, K. Satzinger, M.-H. Chou, A. Bienfait, C. Conner, É. Dumur, J. Grebel, G. Peairs, R. Povey, *et al.*, *Nature Physics* **15**, 741 (2019).
- [6] F. Arute, K. Arya, R. Babbush, D. Bacon, J. C. Bardin, R. Barends, R. Biswas, S. Boixo, F. G. Brandao, D. A. Buell, *et al.*, *Nature* **574**, 505 (2019).
- [7] A. I. Lvovsky, B. C. Sanders, and W. Tittel, *Nature photonics* **3**, 706 (2009).
- [8] J. L. O’Brien, A. Furusawa, and J. Vučković, *Nature Photonics* **3**, 687 (2009).
- [9] N. Lauk, N. Sinclair, S. Barzanjeh, J. P. Covey, M. Saffman, M. Spiropulu, and C. Simon, *Quantum Science and Technology* **5**, 020501 (2020).
- [10] N. J. Lambert, A. Rueda, F. Sedlmeir, and H. G. Schwefel, *Advanced Quantum Technologies* **3**, 1900077 (2020).
- [11] Z.-L. Xiang, S. Ashhab, J. You, and F. Nori, *Reviews of Modern Physics* **85**, 623 (2013).
- [12] J. I. Cirac, P. Zoller, H. J. Kimble, and H. Mabuchi, *Physical Review Letters* **78**, 3221 (1997).
- [13] H. J. Kimble, *Nature* **453**, 1023 (2008).
- [14] R. Schoelkopf and S. Girvin, *Nature* **451**, 664 (2008).
- [15] C. Monroe, R. Raussendorf, A. Ruthven, K. Brown, P. Maunz, L.-M. Duan, and J. Kim, *Physical Review A* **89**, 022317 (2014).
- [16] C. Zhong, Z. Wang, C. Zou, M. Zhang, X. Han, W. Fu, M. Xu, S. Shankar, M. H. Devoret, H. X. Tang, *et al.*, *Physical Review Letters* **124**, 010511 (2020).
- [17] S. Blum, C. O’Brien, N. Lauk, P. Bushev, M. Fleischhauer, and G. Morigi, *Physical Review A* **91**, 033834 (2015).
- [18] B. T. Gard, K. Jacobs, R. McDermott, and M. Saffman, *Physical Review A* **96**, 013833 (2017).
- [19] J. Han, T. Vogt, C. Gross, D. Jaksch, M. Kiffner, and W. Li, *Physical review letters* **120**, 093201 (2018).
- [20] D. Petrosyan, K. Mølmer, J. Fortágh, and M. Saffman, *New Journal of Physics* **21**, 073033 (2019).
- [21] S. Barzanjeh, M. Abdi, G. J. Milburn, P. Tombesi, and D. Vitali, *Physical Review Letters* **109**, 130503 (2012).
- [22] J. Bochmann, A. Vainsencher, D. D. Awschalom, and A. N. Cleland, *Nature Physics* **9**, 712 (2013).
- [23] R. W. Andrews, R. W. Peterson, T. P. Purdy, K. Cicak, R. W. Simmonds, C. A. Regal, and K. W. Lehnert, *Nature Physics* **10**, 321 (2014).
- [24] K. C. Balram, M. I. Davanço, J. D. Song, and K. Srinivasan, *Nature photonics* **10**, 346 (2016).
- [25] A. Higginbotham, P. Burns, M. Urmey, R. Peterson, N. Kampel, B. Brubaker, G. Smith, K. Lehnert, and C. Regal, *Nature Physics* **14**, 1038 (2018).
- [26] L. Shao, M. Yu, S. Maity, N. Sinclair, L. Zheng, C. Chia, A. Shams-Ansari, C. Wang, M. Zhang, K. Lai, *et al.*, *Optica* **6**, 1498 (2019).
- [27] M. Forsch, R. Stockill, A. Wallucks, I. Marinković, C. Gärtner, R. A. Norte, F. van Otten, A. Fiore, K. Srinivasan, and S. Gröblacher, *Nature Physics* **16**, 69 (2020).
- [28] X. Han, W. Fu, C. Zhong, C.-L. Zou, Y. Xu, A. Al Sayem, M. Xu, S. Wang, R. Cheng, L. Jiang, *et al.*, *Nature communications* **11**, 3237 (2020).

- [29] M. Mirhosseini, A. Sipahigil, M. Kalaei, and O. Painter, *Nature* **588**, 599 (2020).
- [30] W. Jiang, C. J. Sarabalis, Y. D. Dahmani, R. N. Patel, F. M. Mayor, T. P. McKenna, R. Van Laer, and A. H. Safavi-Naeini, *Nature communications* **11**, 1166 (2020).
- [31] C. O'Brien, N. Lauk, S. Blum, G. Morigi, and M. Fleischhauer, *Physical review letters* **113**, 063603 (2014).
- [32] L. A. Williamson, Y.-H. Chen, and J. J. Longdell, *Physical review letters* **113**, 203601 (2014).
- [33] R. Hisatomi, A. Osada, Y. Tabuchi, T. Ishikawa, A. Noguchi, R. Yamazaki, K. Usami, and Y. Nakamura, *Physical Review B* **93**, 174427 (2016).
- [34] N. Zhu, X. Zhang, X. Han, C.-L. Zou, C. Zhong, C.-H. Wang, L. Jiang, and H. X. Tang, *Optica* **7**, 1291 (2020).
- [35] M. Tsang, *Physical Review A* **81**, 063837 (2010).
- [36] M. Tsang, *Physical Review A* **84**, 043845 (2011).
- [37] C. Javerzac-Galy, K. Plekhanov, N. Bernier, L. D. Toth, A. K. Feofanov, and T. J. Kippenberg, *Physical Review A* **94**, 053815 (2016).
- [38] L. Fan, C.-L. Zou, R. Cheng, X. Guo, X. Han, Z. Gong, S. Wang, and H. X. Tang, *Science advances* **4**, eaar4994 (2018).
- [39] W. Hease, A. Rueda, R. Sahu, M. Wulf, G. Arnold, H. G. Schwefel, and J. M. Fink, *PRX Quantum* **1**, 020315 (2020).
- [40] W. Fu, M. Xu, X. Liu, C.-L. Zou, C. Zhong, X. Han, M. Shen, Y. Xu, R. Cheng, S. Wang, *et al.*, arXiv preprint arXiv:2010.11392 (2020).
- [41] R. Weis and T. Gaylord, *Applied Physics A* **37**, 191 (1985).
- [42] T. P. McKenna, J. D. Witmer, R. N. Patel, W. Jiang, R. V. Laer, P. Arrangoiz-Arriola, E. A. Wollack, J. F. Herrmann, and A. H. Safavi-Naeini, *Optica* **7**, 1737 (2020).
- [43] J. Holzgrafe, N. Sinclair, D. Zhu, A. Shams-Ansari, M. Colangelo, Y. Hu, M. Zhang, K. K. Berggren, and M. Lončar, *Optica* **7**, 1714 (2020).
- [44] J. Holzgrafe, N. Sinclair, D. Zhu, A. Shams-Ansari, M. Colangelo, Y. Hu, M. Zhang, K. K. Berggren, and M. Loncar, in *CLEO: QELS-Fundamental Science* (Optical Society of America, 2020) pp. FTh4D-5.
- [45] J. Lisenfeld, A. Bilmes, S. Matityahu, S. Zanker, M. Marthaler, M. Schechter, G. Schön, A. Shnirman, G. Weiss, and A. V. Ustinov, *Scientific reports* **6**, 23786 (2016).
- [46] D. Niepce, J. J. Burnett, M. G. Latorre, and J. Bylander, *Superconductor Science and Technology* **33**, 025013 (2020).
- [47] M. Zhang, C. Wang, Y. Hu, A. Shams-Ansari, T. Ren, S. Fan, and M. Lončar, *Nature Photonics* **13**, 36 (2019).
- [48] M. Soltani, M. Zhang, C. Ryan, G. J. Ribeill, C. Wang, and M. Loncar, *Physical Review A* **96**, 043808 (2017).
- [49] Y. Xu, A. A. Sayem, C.-L. Zou, L. Fan, R. Cheng, and H. X. Tang, *Opt. Lett.* **46**, 432 (2021).
- [50] Y. Xu, M. Shen, J. Lu, J. Surya, A. A. Sayem, and H. X. Tang, Mitigating photorefractive effect in thin-film lithium niobate microring resonators (2020), arXiv:2012.12671.
- [51] L. He, M. Zhang, A. Shams-Ansari, R. Zhu, C. Wang, and L. Marko, *Optics letters* **44**, 2314 (2019).
- [52] M. Xu, X. Han, C.-L. Zou, W. Fu, Y. Xu, C. Zhong, L. Jiang, and H. X. Tang, *Physical Review Letters* **124**, 033602 (2020).
- [53] R. Riedinger, A. Wallucks, I. Marinković, C. Löschnauer, M. Aspelmeyer, S. Hong, and S. Gröblacher, *Nature* **556**, 473 (2018).
- [54] R. Riedinger, S. Hong, R. A. Norte, J. A. Slater, J. Shang, A. G. Krause, V. Anant, M. Aspelmeyer, and S. Gröblacher, *Nature* **530**, 313 (2016).

Figures

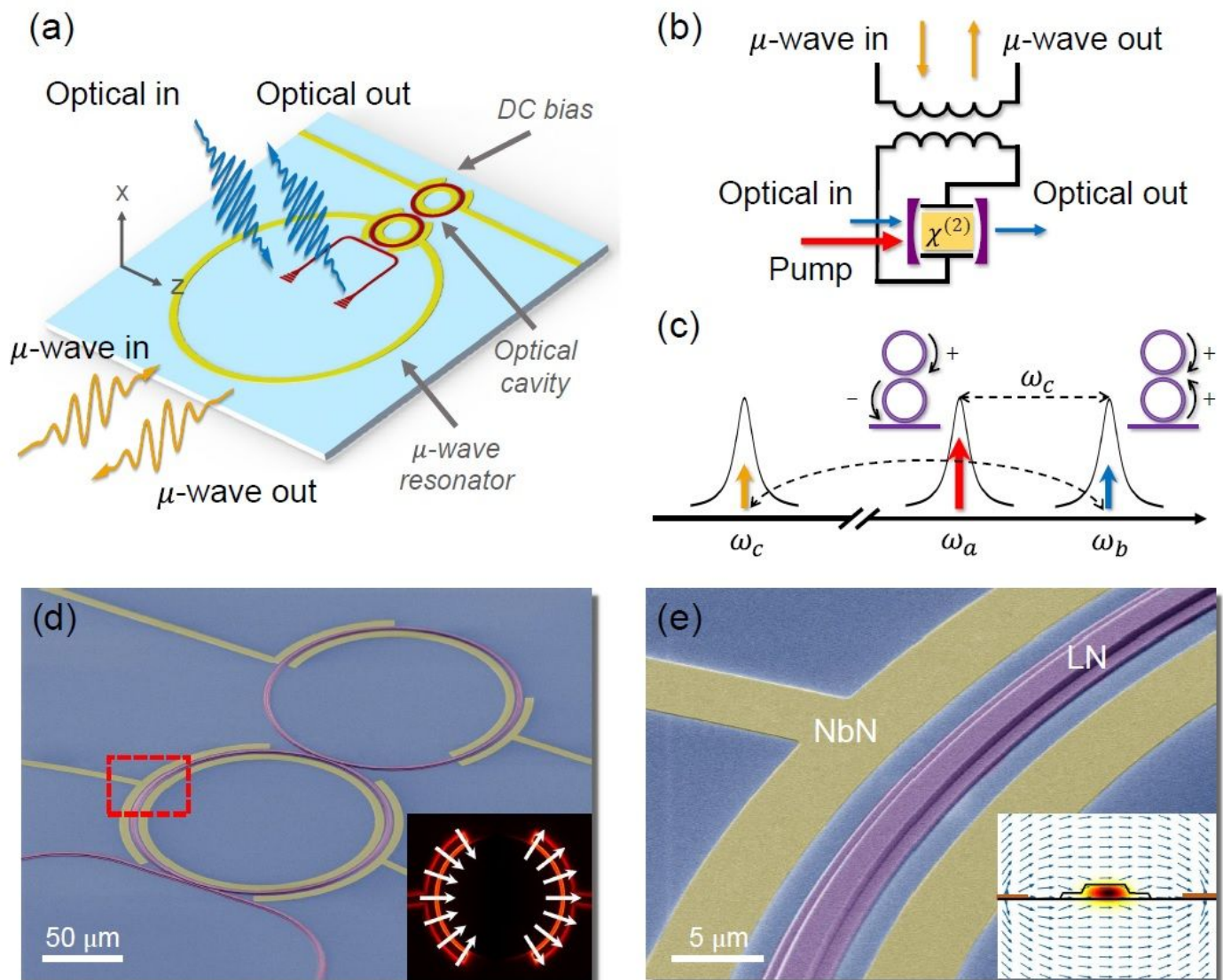


Figure 1

(a) Schematic layout of the TFLN EO converter, where two strongly coupled microring resonators (red) are cointegrated with an planar superconducting resonator (yellow). DC electrodes are utilized for on-chip tuning of the optical modes. (b) Circuit representation of the cavity EO system. The capacitor plate of the lumped-element microwave resonator is coupled to the $\chi^{(2)}$ optical cavity. (c) Three wave-mixing EO conversion process. The optical doublet corresponds to the symmetric and anti-symmetric supermodes of the coupled microrings. A strong pump (red) at the anti-symmetric mode frequency parametrically stimulates the bidirectional conversion between signal photons in the symmetric mode (blue) and the microwave mode (yellow). (d) and (e) False-color scanning electron microscope images of the EO converter device. Insets show the electric field profiles of interacting optical and microwave modes.

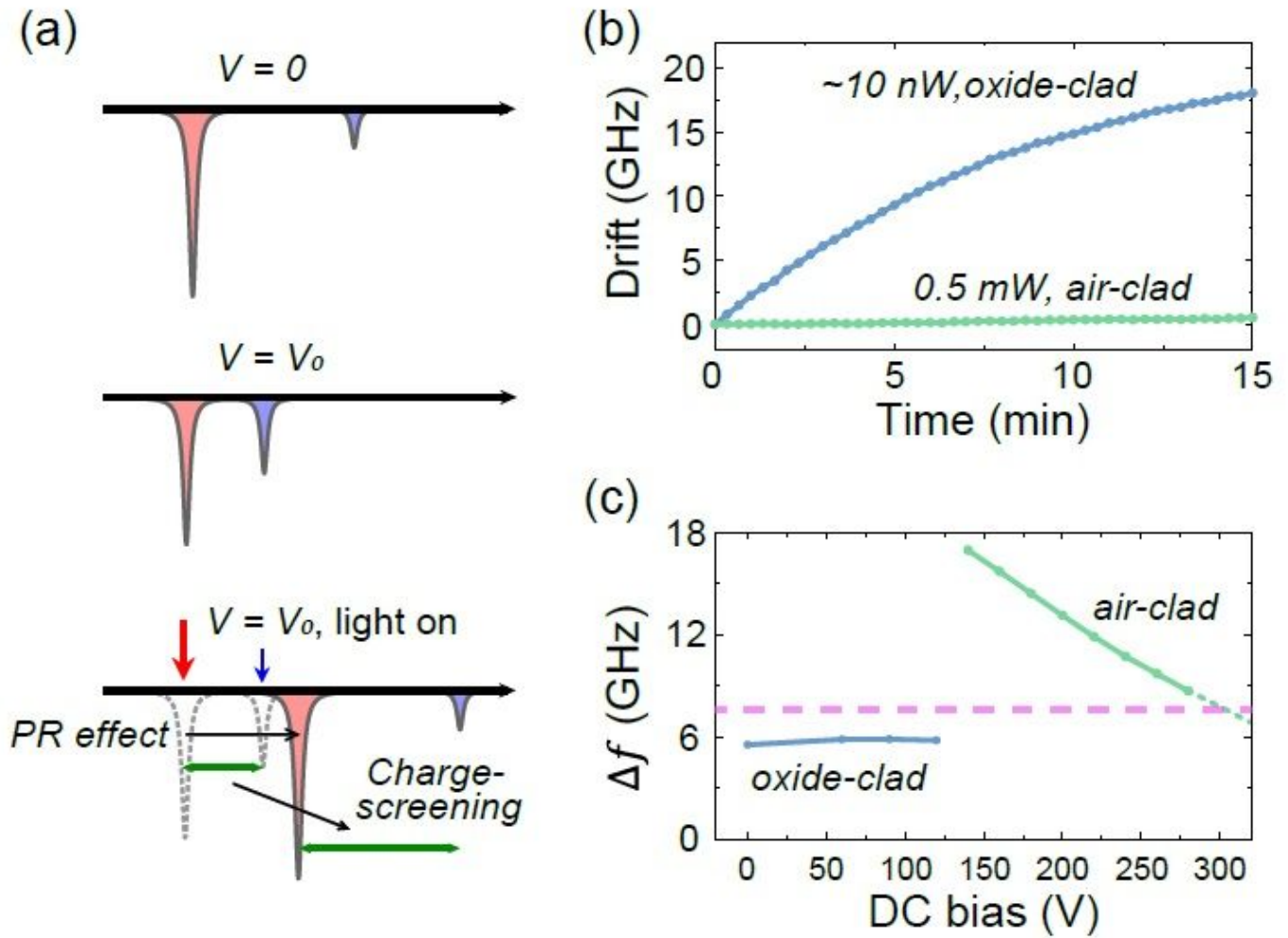


Figure 2

(a) Illustration of the PR-induced resonance instability resulting from a combination of absolute frequency shift and cancellation of voltage tunability after illumination. (b) The measured resonance frequency shift at zero-bias voltage after light illumination of oxide-clad (blue) and air-clad (green) architecture. (c) The optical supermode splitting Δf as a function of DC bias for oxide-clad (blue) and air-clad (green) devices. The target microwave frequency is marked as a dashed line.

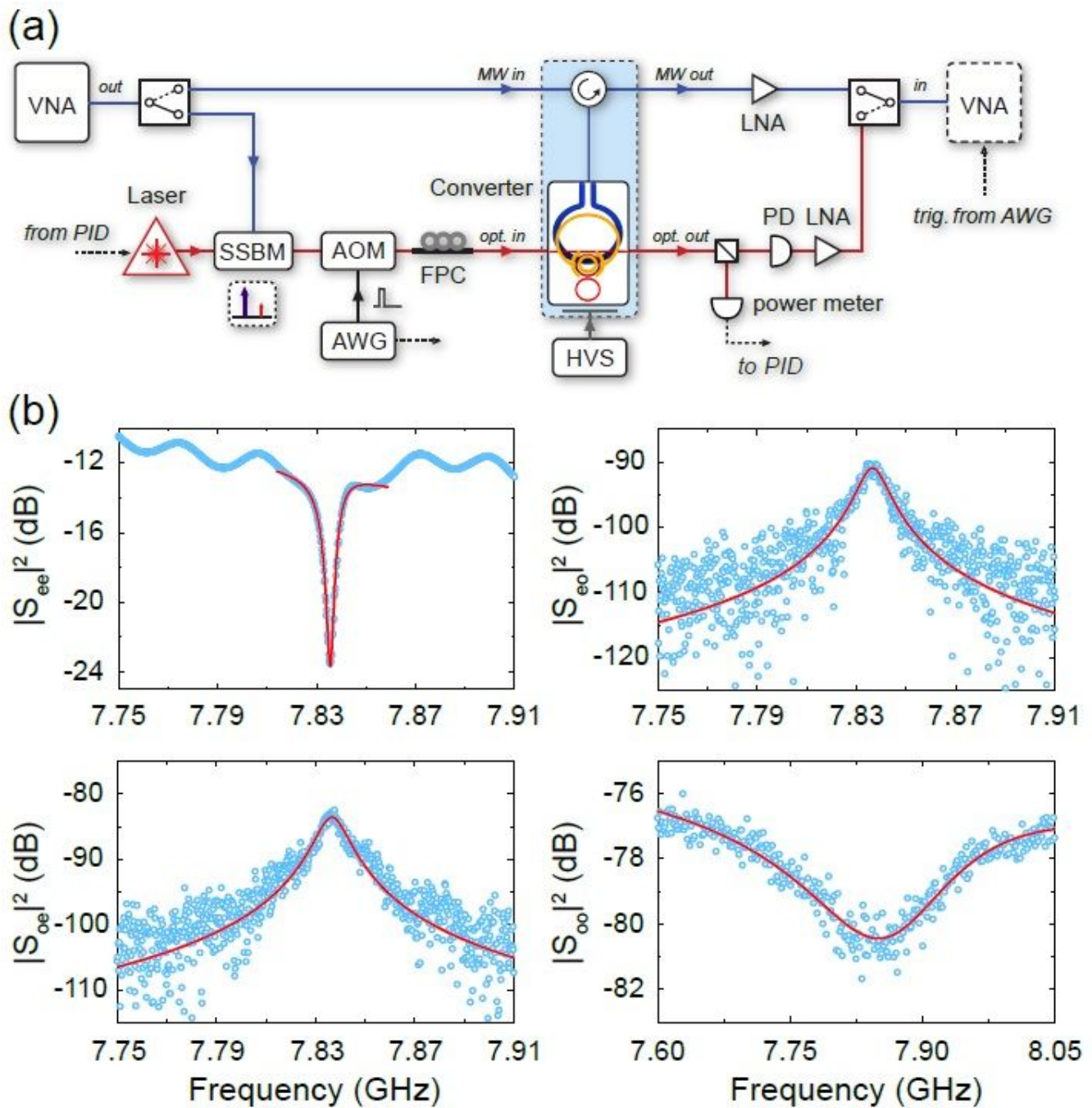


Figure 3

(a) Measurement setup. The output of a vector network analyzer (VNA) is sent to the device either as the microwave input or as the optical input through a singlesideband modulator (SSBM). For quasi-CW measurements, the pump is gated by an acoustic-optic modulator (AOM) driven by an arbitrary wave generator (AWG), which also triggers VNA. The pump is locked to the optical cavity with a PID controller. FPC: Fiber polarization controller. PD: photodetector. LNA: low-noise amplifier. HVS: high voltage source.

(b) Measured microwave reflection S_{ee} , optical-to-microwave conversion S_{eo} , microwave-to-optical

conversion S_{oe} and optical reflection S_{oo} . The peak pump power is 12:0dBm in the waveguide and all matrix coefficients are normalized to the VNA output.

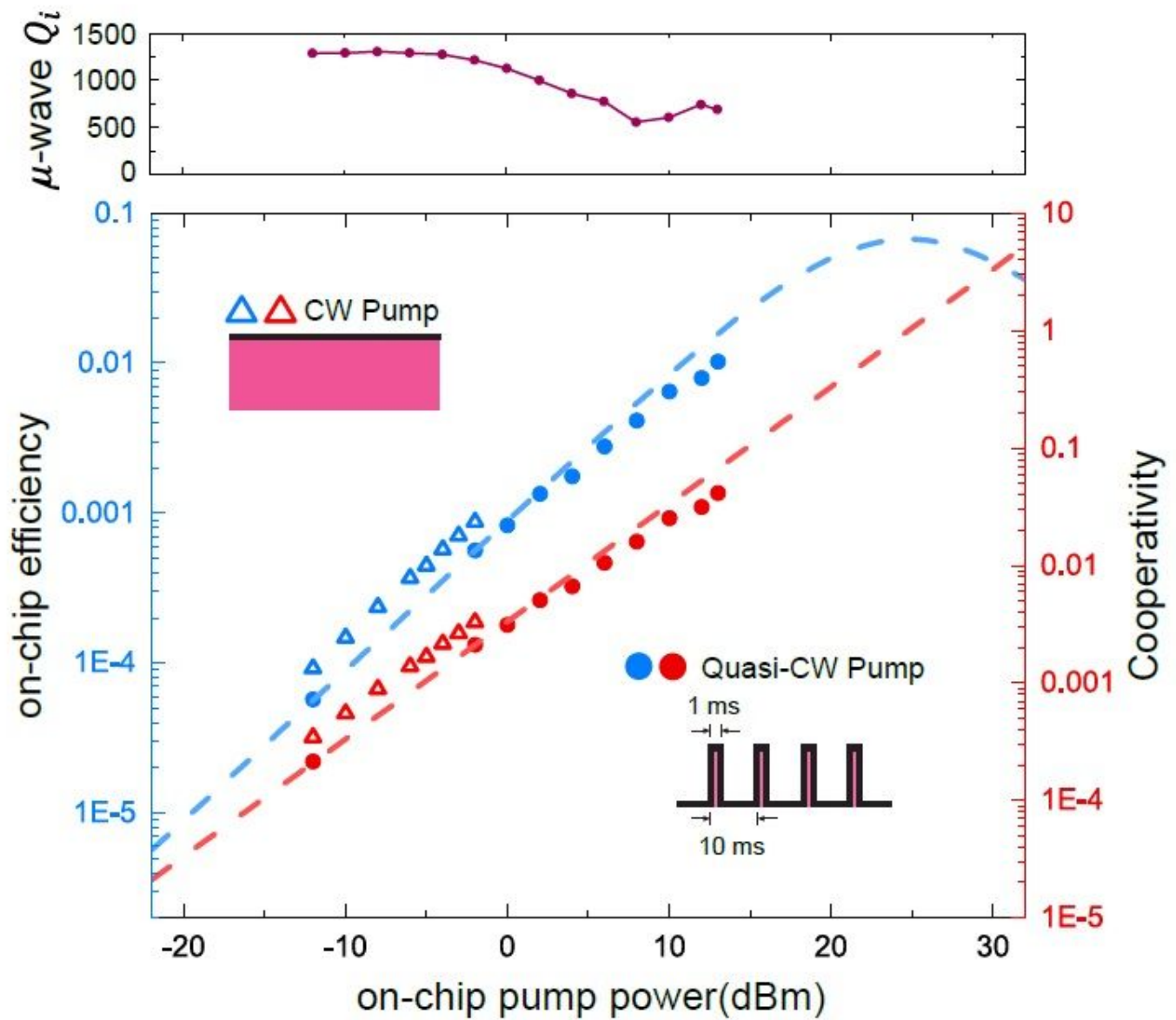


Figure 4

On-chip conversion efficiency (blue) and cooperativity (red) as a function of the peak pump power in the input waveguide. The discontinuity in the CW and pulsed pump data is due to switching to different pairs of optical modes during the measurements. The maximum conversion efficiency is recorded with a peak pump power of 13:0 dBm. The dashed lines are the theoretical predictions obtained from the data measured with a pulsed pump. The measured intrinsic microwave Q under different optical pump powers are presented in the upper panel.

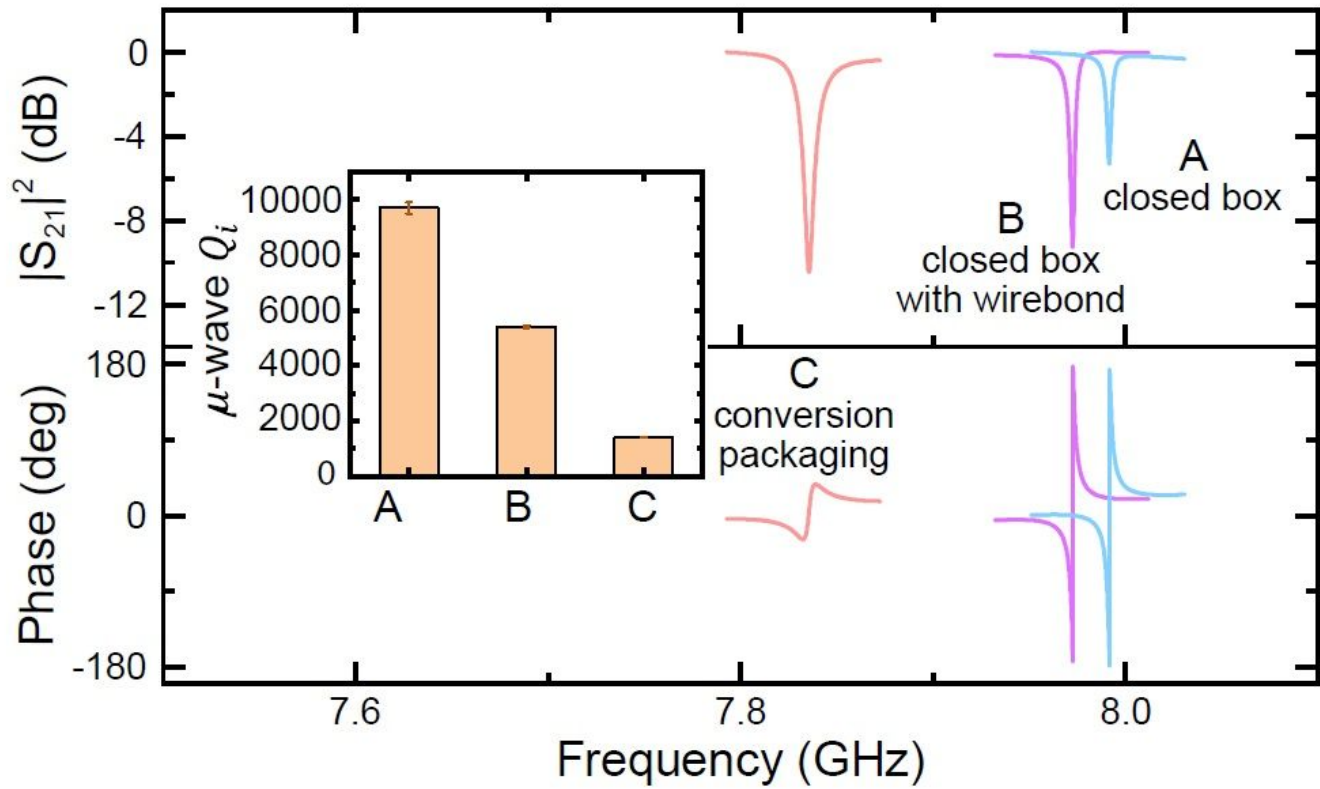


Figure 5

Microwave reflection spectrum of the device (A) in a closed copper box (B) in a closed copper box with wire bonds (C) packaged with fiber-array for conversion measurement. The inset shows the fitted intrinsic microwave quality factors.